

# Nonlinear phononics in Bi<sub>2</sub>Te<sub>3</sub> from first-principles

A. Levchuk,\* R. Busselez, G. Vaudel, P. Ruello, V. Juvé, and B. Arnaud†

*Institut des Molécules et Matériaux du Mans, UMR CNRS 6283,*

*Le Mans université, 72085 Le Mans, France, EU*

(Dated: January 9, 2025)

Density Functional Theory (DFT) calculations not only allow to predict the vibrational and optical properties of solids but also to understand and disentangle the mechanisms playing a key role in the generation of coherent optical phonons. Recent experiments performed on a Bi<sub>2</sub>Te<sub>3</sub> nanofilm have shown that a THz pulse launches at least a coherent A<sub>1g</sub><sup>1</sup> phonon as the transient transmittance measured using an isotropic detection scheme displays oscillations with a frequency matching the frequency of the A<sub>1g</sub><sup>1</sup> mode measured in Raman experiments. Such an observation can be explained by invoking either a sum frequency process or cubic/quartic phonon-phonon couplings as considered for Bi<sub>2</sub>Se<sub>3</sub>, a parent compound of Bi<sub>2</sub>Te<sub>3</sub>. By resorting to group theory and calculating energy surfaces from first-principles, the main phonon-phonon couplings can be identified. Furthermore, a minimal model can be built to compute the dynamics of the Raman active modes coupled to the infrared active mode driven by the experimental THz pulse. Our model firmly establishes that cubic phonon-phonon interactions are relevant as the agreement between the computed and experimental transmittance is noteworthy.

Advances in THz physics[1], through the generation[2–5] and detection[6–8] of intense THz pulses, have revolutionized the field of condensed matter physics, where the concept of quasiparticles like excitons, magnons, and phonons, is essential. Indeed, low energy excitations can be targeted to induce non-equilibrium quantum states with novel properties that challenge our understanding of solid state physics. Phonons are quasiparticles with a finite lifetime essentially arising from phonon-phonon interactions at high temperature. These interactions, which provide a natural explanation for the finite thermal conductivity of solids, are leveraged in the blooming field of nonlinear phononics[9–11]. In a few words, a THz pulse drives resonantly or nonresonantly one or more infrared (IR) active modes which in turn are coupled to other symmetry allowed modes. To cite few examples[12], nonlinear phonon-phonon mixing has been exploited to induce insulator-to-metal transition in a manganite[13], to reverse the polarization in a ferroelectric[14] or even to induce ferrimagnetism in an antiferromagnet by mimicking the effect of an externally applied strain[15].

In this Letter, we provide a theoretical interpretation of the pump-probe experiments performed on a n-doped Bi<sub>2</sub>Te<sub>3</sub> nanofilm deposited on a mica substrate[16–18]. As shown in Fig. 1(a), the free electrons are driven by the THz pump pulse shown in the inset and give rise to a steep increase of the transmittance followed by a decay arising from electron-phonon scattering events[19, 20] on a time scale  $\sim 4$  ps. The fast oscillatory component with a frequency  $\sim 1.86$  THz, that is surimposed on the decay, can be ascribed to the coherently driven A<sub>1g</sub><sup>1</sup> optical phonon seen in Raman experiments[21, 22]. It's worth remarking that our isotropic detection scheme is only

sensitive to the symmetry preserving modes, namely the A<sub>1g</sub> modes. Interestingly, Melnikov *et al*[23] performed similar experiments on a Bi<sub>2</sub>Se<sub>3</sub> nanofilm and observed the A<sub>1g</sub><sup>1</sup> mode by measuring the transient transmittance as well as both the E<sub>u</sub><sup>1</sup>, E<sub>g</sub><sup>1</sup> and E<sub>g</sub><sup>2</sup> modes by measuring the transient polarization rotation. The generation of the E<sub>g</sub><sup>2</sup> (A<sub>1g</sub><sup>1</sup> and E<sub>g</sub><sup>1</sup>) mode was tentatively explained by invoking a third (fourth) order coupling with the E<sub>u</sub><sup>1</sup> mode driven by the THz pulse. Thus, the question arises to know whether quartic interactions, as speculated for Bi<sub>2</sub>Se<sub>3</sub> which is a parent compound of Bi<sub>2</sub>Te<sub>3</sub>, might explain the generation of the A<sub>1g</sub><sup>1</sup> phonon mode seen in our experiments. *Ab initio* calculations have already shown their strength in disentangling the many different processes occurring in the field of ultrafast physics[24–28]. Furthermore, they offer not only the possibility to identify relevant mechanisms by evaluating the phonon-phonon coupling terms[10, 29] but also provide the less explored opportunity to simulate the detection process, allowing a direct comparison with the experimental results.

Bi<sub>2</sub>Te<sub>3</sub> crystallizes in a rhombohedral structure, also called A7 structure, with a trigonal axis parallel to  $\mathbf{c} = \mathbf{a}_1 + \mathbf{a}_2 + \mathbf{a}_3$ , where  $\mathbf{a}_1$ ,  $\mathbf{a}_2$  and  $\mathbf{a}_3$  span the unit cell[30–32]. All the calculations, which include spin-orbit coupling[33], are performed for the experimental lattice parameters[30] within the framework of the local density approximation (LDA) as implemented in the ABINIT code[34, 35]. As the primitive cell contains five atoms, there are 15 lattice dynamical modes at  $\mathbf{q} = \mathbf{0}$ , three of which are acoustic modes. Group theory classifies the remaining 12 optical modes into 2 A<sub>1g</sub> (R), 2 E<sub>g</sub> (R), 2 A<sub>2u</sub> (IR) and 2 E<sub>u</sub> (IR) modes, where R and IR refer to Raman and infrared active modes respectively. The dynamical matrix is computed using density functional perturbation theory[36] and diagonalized to get the zone center frequencies shown in Fig. 1(b) as downward (upward) arrows for IR (R) active modes. The overall agree-

\*Present address: Laboratoire des Solides Irradiés, UMR 7642 CEA-CNRS, Ecole Polytechnique, France, EU.

†e-mail: brice.arnaud@univ-lemans.fr

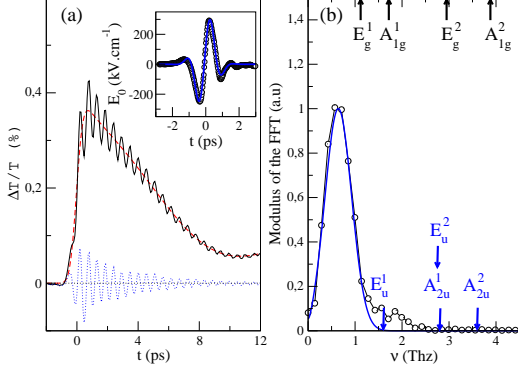


FIG. 1: (a) Transient optical transmittance  $\Delta T/T$  (black line) at 400 nm (the probe pulse duration is  $\sim 165$  fs) following a THz pump excitation ( $\mathbf{E} \perp \mathbf{c}$  with a peak field strength  $\sim 300$   $\text{kV}\cdot\text{cm}^{-1}$ ) on a  $\text{Bi}_2\text{Te}_3$  nanofilm[17, 18]. The contribution of both free carriers and strain to  $\Delta T/T$  is indicated as a red dashed line while the contribution of the coherent optical phonon is displayed as a blue dotted line. The THz electric field[18] (open circles) is shown in the inset and compared with a fit to an analytical function (solid blue line). (b) Fourier transforms of both the experimental (open circles) and analytical (solid blue line) THz waveform together with the computed zone center frequencies at the LDA level shown as vertical arrows[32].

ment between theory[32] and experiment[37] is reasonable. The eigenvectors of the zone center dynamical matrix as well as the Born effective charges[32, 38, 39] are key ingredients[40] to evaluate the mode effective charges. The mode effective charges, which are non zero only for IR active modes, are respectively equal  $-36.3$  and  $-3.92$  for the  $E_u^1$  and  $E_u^2$  modes[18]. It's worth highlighting that these values show that the  $E_u^1$  modes are strongly coupled with an in-plane electric field. ( $\mathbf{E} \perp \mathbf{c}$ ) while the  $E_u^2$  modes are much less coupled. In the following, the mode effective charge for the  $E_u^1$  modes is denoted as  $Z_\perp$ .

We now focus on the coupling between the  $E_u^1$  modes and other modes, whose irreducible representation are respectively denoted  $\Gamma_{E_u}$  and  $\Gamma$ . Group theory tells us that the modes that are potentially coupled to the IR modes are such that the symmetrized representation  $[\Gamma_{E_u} \otimes \Gamma_{E_u}]_s$  contains  $\Gamma$ [41]. As the point group of  $\text{Bi}_2\text{Te}_3$  is  $D_{3d}$ , it's easy to show that  $[\Gamma_{E_u} \otimes \Gamma_{E_u}]_s = A_{1g} \oplus E_g$ . Thus, the energy of the crystal per unit cell, denoted as  $V$ , is computed as a function of  $Q_{R,0}$  (coordinate of the  $A_{1g}^1$  mode),  $Q_{R,i}$  (coordinates of the  $E_g^1$  mode) and  $Q_{IR,i}$  (coordinates of the  $E_u^1$  mode), where  $i = 1, 2$  since the  $E_g^1$  and  $E_u^1$  modes are two-fold degenerate. To alleviate the notations, the upper index for both the  $E_g^1$  and  $E_u^1$  modes is suppressed in the following but remains implicit. The full computation of  $V$  is cumbersome since it depends on five coordinates. However,  $V$  must necessarily be invariant by all elements of the point group, leading to a substantial simplification. Let  $Q_{IR,1}$

and  $Q_{IR,2}$  be the coordinates of the  $E_u$  mode whose polarization respectively lies along one of the two-fold axis (x-axis) and one of the mirror plane (y-axis). Then, we choose the coordinates  $Q_{R,1}$  and  $Q_{R,2}$  such that they respectively transform as  $Q_{IR,2}^2 - Q_{IR,1}^2$  and  $Q_{IR,1}Q_{IR,2}$ . With such a choice, the energy  $V$  reads:

$$V/M = \frac{1}{2}\Omega_{R,0}^2 Q_{R,0}^2 + \frac{1}{2}\Omega_R^2 Q_R^2 + \frac{1}{2}\Omega_{IR}^2 Q_{IR}^2 + bQ_{IR}^4 + g_1 [Q_{R,1} (Q_{IR,2}^2 - Q_{IR,1}^2) + 2Q_{IR,1}Q_{IR,2}Q_{R,2}] + g_0 Q_{R,0} Q_{IR}^2, \quad (1)$$

where  $Q_{R/IR}^2 = \sum_{i=1}^2 Q_{R/IR,i}^2$  and  $\Omega_{R,0}$ ,  $\Omega_R$  and  $\Omega_{IR}$  are respectively the angular frequencies of the  $A_{1g}$ ,  $E_g$  and  $E_u$  modes. Here, the first line represents the harmonic contributions including the quartic term for the IR active mode and the last two lines the cubic terms, where  $g_0$  ( $g_1$ ) denotes the coupling constant between the  $E_u$  modes and the  $A_{1g}$  ( $E_g$ ) modes. The coupling constants entering Eq. 1 are obtained from a simultaneous least squares fit of the two energy surfaces  $V(Q_{IR,1}, Q_{R,i})$  computed at the LDA level[18], where  $i = 0$  ( $A_{1g}$  mode) and  $i = 1$  ( $E_g$  mode).

Neglecting the feedback effect of the Raman active modes on the IR active mode as well as the renormalization of the IR mode arising from the quartic term leads to the following equations of motion:

$$\begin{cases} \ddot{Q}_{IR,\alpha} + 2\gamma_{IR}\dot{Q}_{IR,\alpha} + \Omega_{IR}^2 Q_{IR,\alpha} = F^\alpha(t)/M \\ \ddot{Q}_{R,i} + 2\gamma_{R,i}\dot{Q}_{R,i} + \Omega_{R,i}^2 Q_{R,i} = F_{R,i}^{anh}/M, \end{cases} \quad (2)$$

for  $\alpha = 1, 2$  and  $i = 0, 1, 2$ . Here,  $\Omega_{R,1} = \Omega_{R,2} = \Omega_R$ ,  $F^\alpha(t) = eZ_\perp E^\alpha(t)$  is the component along  $\alpha$  of the force driving the IR active mode,  $F_{R,0}^{anh} = -Mg_0 Q_{IR}^2$ ,  $F_{R,i}^{anh} = -Mg_1 [\delta_{i,1} (Q_{IR,2}^2 - Q_{IR,1}^2) + 2\delta_{i,2} Q_{IR,1}Q_{IR,2}]$ . Note that the forces arising from two-photon direct excitation of the Raman active modes[42–44] are neglected.

The time profile of the THz pulse measured by an electro-optic method[7, 8] is displayed in the inset of Fig. 1(a) and well fitted by  $E_0(t) = E_0 \sin[\omega_0 t + \Phi_0] \exp[-t^2/\sigma^2]$  where  $\omega_0/2\pi = 0.64$  THz,  $\sigma = 0.79$  ps,  $\Phi_0 = 0.117\pi$  and  $E_0 \sim 340$   $\text{kV}\cdot\text{cm}^{-1}$ [18]. The components of the THz pulse inside the  $\text{Bi}_2\text{Te}_3$  nanofilm are given by  $E^\alpha(t) = pE_0(t) [\cos(\Phi)\delta_{\alpha,1} + \sin(\Phi)\delta_{\alpha,2}]$ , where  $\Phi$  is the angle between the electric field and the x-axis and  $p \sim 2/(1 + n_{\text{mica}}) \sim 0.57$  since  $n_{\text{mica}} \sim 2.5$  for  $\omega_0/2\pi \sim 0.6$  THz[45]. It's worth outlining that the electric field inside the nanofilm is neither dependent on the nanofilm thickness nor on the dielectric properties of the nanofilm as the THz pulse wavelength is much larger than the film thickness.

The set of coupled equations are solved using a fourth order Runge-Kutta scheme with a time step of one fs. The only unknown parameters are  $\gamma_{IR/R,i}$  that are related to the inverse phonon lifetimes. We choose  $\gamma_{IR} \sim 0.44$   $\text{ps}^{-1}$  as this value allows to reproduce the IR spectra of  $\text{Bi}_2\text{Te}_3$ [32] and consider that  $\gamma_{R,0} \sim 0.28$   $\text{ps}^{-1}$  as the full width at half maximum of the  $A_{1g}$  mode is  $\sim 3$   $\text{cm}^{-1}$

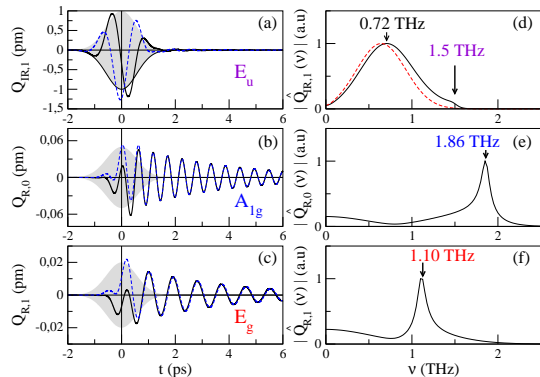


FIG. 2: Calculated time evolution of the  $E_u^1$  (a),  $A_{1g}^1$  (b) and  $E_g^1$  (c) mode coordinates following the arrival of a THz pulse polarized along the  $x$ -axis ( $\Phi = 0$ ) with an amplitude  $\sim 193 \text{ kV}\cdot\text{cm}^{-1}$  inside the  $\text{Bi}_2\text{Te}_3$  nanofilm ( $E_0 \sim 340 \text{ kV}\cdot\text{cm}^{-1}$ ). The solid lines represent  $Q_{IR,1}$ ,  $Q_{R,0}$  and  $Q_{R,1}$  for  $\Phi_0 = 0.117\pi$  while the dashed lines represent  $Q_{IR,1}$ ,  $-Q_{R,0}$  and  $-Q_{R,1}$  for  $\Phi_0 = 0.117\pi + \pi/2$ . The grey shaded areas represent the envelope of the THz pulse. The normalized Fourier Transforms (FT) of the phonon coordinates  $Q$ , denoted as  $\hat{Q}$ , are shown in panels (d), (e) and (f) for  $\Phi_0 = 0.117\pi$ . The FT of the THz electric field is shown as a dashed line in panel (d).

at room temperature[46]. As no data is available for the  $E_g$  mode, we assume that the inverse phonon lifetime for this mode is the same than for the  $A_{1g}$  mode.

In Fig. 2, we report the dynamics of the  $E_u$ ,  $A_{1g}$  and  $E_g$  modes for a THz pulse polarized along the  $x$ -axis. As shown in panel (a), the  $Q_{IR,1}$  coordinate is phase shifted from  $\pi$  ( $Z_{\perp} < 0$ ) with respect to the THz pulse shown in the inset of Fig. 1(a) and displays tiny oscillations at the frequency of the  $E_u$  mode that are seen as a small bump in the Fourier Transform (FT) of  $Q_{IR,1}$ , denoted as  $\hat{Q}_{IR,1}(\nu)$  and shown in panel (d). Such a behaviour is easy to understand as the THz pulse is non-resonant with the IR mode[18]. As shown in Fig. 2(b), the symmetry preserving  $Q_{R,0}$  mode oscillates around a displaced equilibrium position during the THz pulse and oscillates around its equilibrium position after. The Fourier transform of the  $Q_{R,0}$  mode, denoted as  $\hat{Q}_{R,0}(\nu)$  and shown in panel (e), displays a peak at 1.86 THz, corresponding to the natural frequency oscillation of the  $A_{1g}$  mode. Reminding that the driving force acting on the  $A_{1g}$  mode is  $F_{R,0}^{anh} = -Mg_0Q_{IR,1}^2$  ( $Mg_0 \sim 0.12 \text{ Ha}\cdot\text{bohr}^{-3}$ ), the  $A_{1g}$  mode is not efficiently driven. Indeed, the maximum value of  $|Q_{R,0}|$  is 0.06 pm for  $\omega_0/2\pi = 0.64 \text{ THz}$ , while reaching 0.14 pm when  $\omega_0/2\pi$  is tuned to half the frequency of the  $A_{1g}$  mode[18]. It's also important to remark that the dynamics of the  $A_{1g}$  mode, unlike the dynamics of the  $E_g$  mode, does not depend on the polarization of the THz field. As shown in Fig. 2(c), the behaviour of the  $Q_{R,1}$  coordinate is similar to the behaviour

of the  $Q_{R,0}$  coordinate. The main difference is that the maximum value of  $|Q_{R,1}|$  is 0.018 pm. Here, the driving force  $F_{R,1}^{anh} = Mg_1Q_{IR,1}^2$  ( $Mg_1 \sim -0.02 \text{ Ha}\cdot\text{bohr}^{-3}$ ) is six times smaller than  $F_{R,0}^{anh}$  but the double of the frequency of the THz mode. It's worth outlining that only the  $Q_{R,1}$  mode is coherently driven when the THz pulse is polarized along the  $x$ -axis ( $\Phi = 0$ ) or  $y$ -axis ( $\Phi = \pi/2$ ) while only the  $Q_{R,2}$  mode is driven when  $\Phi = \pi/4, 3\pi/4$ . Thus, the polarization of the THz pulse offers the unique opportunity to steer the dynamics of the  $E_g$  mode and especially to transiently lower the crystal symmetry to  $2/m$  ( $\bar{1}$ ) when  $Q_{R,1}$  ( $Q_{R,2}$ ) is coherently driven. Interestingly, the symmetry lowering is enhanced and lasts longer than  $\sigma \sim 0.8 \text{ ps}$  when the THz pulse is resonant with the  $E_u$  mode[18].

It's also tempting to play with the carrier envelope phase  $\Phi_0$  of the THz pulse. The maximum values of the phonon coordinates are only slightly affected by  $\Phi_0$  ruling out the idea to adjust  $\Phi_0$  in order to enhance the amplitudes of the  $A_{1g}$  and  $E_g$  modes. However, it's easy to play with the phases of  $Q_{R,i}$ , where  $i = 0, 1, 2$ . We expect the long time dynamics of these modes to be well described by  $Q_{R,i}^{long}(t, \Phi_0) = A_{R,i} \cos[\hat{\Omega}_{R,i}t + f_i(\Phi_0)]$ , where  $f_i(\Phi_0 \pm \pi) = f_i(\Phi_0) \pm 2\pi$ . Indeed, a change in the sign of the THz pulse does not affect the long time dynamics of the  $Q_{R,i}$  modes as the driving forces remain unchanged. The only way to satisfy the previous equation is to impose  $f_i(\Phi_0) = 2\Phi_0 + \Phi_{R,i}$ . This property has been checked in our numerical calculations. As shown in Fig. 2, the long time dynamics of the  $A_{1g}$  and  $E_g$  phonons corresponding to  $\Phi_0 = 0.117\pi + \pi/2$  (dashed curves) are phase shifted from  $\pi$  with respect to the dynamics corresponding to  $\Phi_0 = 0.117\pi$  (solid curves). Interestingly, the coherent phonon dynamics in diamond arising from a THz sum-frequency process displays a similar dependence on the carrier envelope phase[42].

It is important to simulate the detection process in order to assess the validity of our approach and confirm that our model captures the most relevant mechanisms. Indeed, we could expect that the optical properties of the  $\text{Bi}_2\text{Te}_3$  nanofilm are modulated by the coherently driven  $A_{1g}$  mode, leading to a variation of the measured transmittance of the heterostructure. Both the computed real and imaginary part of the dielectric function  $\epsilon_{\perp}(\omega)$  at the Random Phase Approximation (RPA) level[32, 47–49] for  $Q_{R,0} = \pm 1.2 \text{ pm}$  are displayed in Fig. 3(a). As  $Q_{R,0}$  increases,  $\text{Im}[\epsilon_{\perp}(\omega)]$  decreases when  $\hbar\omega \leq 1.5 \text{ eV}$ . Thus, the oscillator strength is transferred to the high energy side as the optical sum rule should be obeyed. When  $Q_{R,0}$  varies from  $-1.2 \text{ pm}$  to  $1.2 \text{ pm}$ , the imaginary part (real part) of  $\epsilon_{\perp}$  varies from 10.60 ( $-9.83$ ) to 11.24 ( $-9.71$ ) for  $\hbar\omega = 3.1 \text{ eV}$ . Hence, the change in the optical index of  $\text{Bi}_2\text{Te}_3$  at the probe wavelength is essentially related to the change in the imaginary part of the dielectric constant.

Our measurements are carried out on a  $\text{Bi}_2\text{Te}_3$

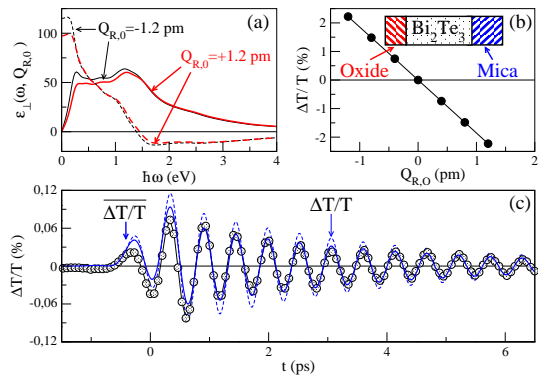


FIG. 3: (a) Computed real (dashed lines) and imaginary part (thin lines) of the dielectric function  $\epsilon_{\perp}$  at the RPA level for an electric field perpendicular to the trigonal axis and for  $Q_{R,0} = \pm 1.2$  pm as a function of the photon energy (in eV). (b) Transmittance  $\Delta T/T = [T(Q_{R,0}) - T(0)]/T(0)$  at 400 nm (wavelength of the probe pulse) computed using a transfer matrix approach[51] for the heterostructure schematically depicted in the inset: The oxide layer,  $\text{Bi}_2\text{Te}_3$  film and mica substrate are respectively 4 nm, 12.2 nm and 17.1  $\mu\text{m}$  thick. The phonon coordinate  $Q_{R,0}$  is varied between -1.2 pm and 1.2 pm with a step of 0.4 pm. (c)  $\Delta T/T$  (dashed blue curve) and  $\overline{\Delta T/T}$  (thick blue curve) as a function of the time delay  $t$  between the probe pulse and the pump THz pulse compared to the oscillatory part (open circles) of the transient measured transmittance shown in Fig.1(a) as a blue dotted line. The experimental value of the THz electric field  $E_0 \sim 340 \text{ kV}\cdot\text{cm}^{-1}$  is used in the simulations and the measured signal is shifted to match the theoretical prediction as the zero time delay is ill-defined in our experiments.

nanofilm deposited on a mica substrate[16–18]. The nanofilm is covered with an oxidized layer whose exact nature remains unknown. However, X-ray photoelectron spectroscopy experiments[16] have shown the presence of Bi-O and Te-O bonds that are the hallmarks of an oxidized layer displaying the properties of a glass[50] which might share some properties with bulk  $\text{Bi}_2\text{O}_3$  and bulk  $\text{TeO}_2$ . Thus, we consider an hypothetical structure schematically depicted in the inset of Fig. 3(b) with an oxidized layer either made of  $\text{Bi}_2\text{O}_3$  or  $\text{TeO}_2$ . Using a transfer matrix approach[51] and the complex refractive index of  $\text{Bi}_2\text{Te}_3$  evaluated at the RPA level[32] as well as the experimental optical index of  $\text{Bi}_2\text{O}_3$ [52],  $\text{TeO}_2$ [53] and mica[54], the relative transmittance  $\Delta T/T$  of both envisioned heterostructures is computed as a function of  $Q_{R,0}$  when the mica layer is treated as an incoherent layer. While the transmittance  $T$  is slightly higher for a  $\text{Bi}_2\text{O}_3$  layer than for a  $\text{TeO}_2$  layer, the

relative transmittance is almost unchanged demonstrating that the very nature of the oxide layer is unimportant. As shown in Fig. 3(b),  $\Delta T/T = \beta Q_{R,0}$ , where  $\beta = -1.85 \text{ pm}^{-1}$ . Because of the finite duration of the probe pulse, what is measured is not  $\Delta T/T = \beta Q_{R,0}(t)$  (see the dashed line in Fig. 3(c)) but rather  $\overline{\Delta T/T} = \beta Q_{R,0} \otimes g_{\sigma}(t)$ , where the phonon coordinate  $Q_{R,0}$  is convoluted with a normalized Gaussian function defined by  $g_{\sigma}(t) = \exp[-t^2/\sigma^2]/\sqrt{\pi\sigma^2}$ . Here, the full width at half maximum (FWHM) is  $2\sigma\sqrt{\ln 2} \sim 165$  fs. As shown in Fig. 3(c), the agreement between theory (thick blue line) and experiment (open circles) is noteworthy especially for time delays larger than  $\sigma \sim 0.8$  ps. The weak discrepancy between theory and experiment for shorter time delays might be due to the imperfect fit of the oscillatory part of the signal[18] or to mechanisms not included in our model.

Our first-principles calculations unravel the mechanisms behind the generation of the  $A_{1g}^1$  phonon in THz excited  $\text{Bi}_2\text{Te}_3$  nanofilms. Indeed, the transient electric field non-resonantly drives the  $E_u^1$  mode which in turn is coupled to both  $A_{1g}^1$  and  $E_g^1$  modes through phonon-phonon interactions arising from cubic terms in the total energy expansion. Thus, the generation of the  $A_{1g}^1$  mode can not be ascribed to quartic terms, as speculated for  $\text{Bi}_2\text{Se}_3$ [23], a parent compound of  $\text{Bi}_2\text{Te}_3$ . Regarding the detection process, we demonstrate that the optical properties of the nanofilm are modulated by the  $A_{1g}$  mode and show that we can achieve a quantitative description of the oscillatory part of the transient transmittance using the characteristics of both pump and probe pulses and, remarkably without introducing any adjustable parameters in our calculations. Furthermore, the atomic displacements can be inferred from *ab initio* calculations without resorting to THz-pump and X-ray probe experiments as done in the study of THz-driven upconversion in  $\text{SrTiO}_3$ [29]. Finally, we predict that a THz pump with a frequency matching the frequency of the  $E_u^1$  mode can transiently lower the symmetry of the system.

## Acknowledgments

We acknowledge GENCI-CINES (project 095096) for high performance computing resources and the funding from the French National Research Agency (ANR) through the EPHONO project (Grant No. ANR-22-CE30-0007). We also thank Dr. K. Balin for providing high quality  $\text{Bi}_2\text{Te}_3$  thin films grown by MBE at the Physics Institute of Silesia University.

[1] T. Kampfrath, K. Tanaka and K. A. Nelson, Resonant and nonresonant control over matter and light by intense

terahertz transients, Nature Photonics **7**, 680 (2013).

[2] K. Reimann, Table-top sources of ultrashort THz pulses,

- Rep. Prog. Phys. **70**, 1597 (2007).
- [3] G. Kh. Kitaeva, Terahertz generation by means of optical lasers, *Laser Phys. Lett.* **5**, 559-576 (2008).
- [4] J. Hebling, K.-L. Yeh, M.C. Hoffmann, B. Bartal and K.A. Nelson, Generation of high-power terahertz pulses by tilted-pulse-front excitation and their application possibilities, *J. Opt. Soc. Am. B* **25**, 6-19 (2008).
- [5] H. Hirori, A. Doi, F. Blanchard, K. Tanaka, Single-cycle terahertz pulses with amplitudes exceeding 1 MV/cm generated by optical rectification in LiNbO<sub>3</sub>, *Appl. Phys. Lett.* **98**, 091106 (2011).
- [6] Q. Wu and X.-C Zhang, Free-space electro-optic sampling of terahertz beams, *Appl. Phys. Lett.* **67**, 3523-3525 (1995).
- [7] Fabian D. J. Brunner, Jeremy A. Johnson, Sebastian Grübel, Andrés Ferrer, Steven L. Johnson, and Thomas Feurer, Distortion-free enhancement of terahertz signals measured by electro-optic sampling. I. Theory *J. Opt. Soc. Am. B* **31**, 904-910 (2014).
- [8] Jeremy A. Johnson, Fabian D. J. Brunner, Sebastian Grübel, Andrés Ferrer, Steven L. Johnson, and Thomas Feurer, Distortion-free enhancement of terahertz signals measured by electro-optic sampling. II. Experiment *J. Opt. Soc. Am. B* **31**, 1035-1040 (2014).
- [9] M. Först, C. Manzoni, S. Kaiser, Y. Tomioka, Y. Tokura, R. Merlin and A. Cavalleri, Non linear phononics as an ultrafast route to lattice control, *Nature Physics* **7**, 854 (2011).
- [10] A. Subedi, A. Cavalleri and A. Georges, Theory of nonlinear phononics for coherent light control of solids, *Physical Review B* **89**, 220301(R) (2014).
- [11] A. S. Disa, T. F. Nova and A. Cavalleri, Engineering crystal structures with light, *Nature Physics* **17**, 1087-1092 (2021).
- [12] D. Nicoletti and A. Cavalleri, Nonlinear light-matter interaction at terahertz frequencies, *Adv. Opt. Photonics* **8**, 401 (2016).
- [13] M. Rini, R. Tobey, N. Dean, J. Itatani, Y. Tomioka, Y. Tokura, R. W. Schoenlein and A. Cavalleri, Control of the electronic phase of a manganite by mode-selective vibrational excitation, *Nature (London)* **449**, 72 (2007).
- [14] R. Mankowsky, A. von Hoegen, M. Först, and A. Cavalleri, Ultrafast Reversal of the Ferroelectric Polarization, *Physical Review Letters* **118**, 197601 (2017).
- [15] A. S. Disa, M. Fechner, T. F. Nova, B. Liu, M. Först, D. Prabhakaran, P. G. Radaelli and A. Cavalleri, Polarizing an antiferromagnet by optical engineering of the crystal field, *Nature Physics* **16**, 937-941 (2020).
- [16] M. Weis, K. Balin, R. Rapacz, A. Nowak, M. Lejman, J. Szade and P. Ruello, Ultrafast light-induced coherent optical and acoustic phonons in few quintuple layers of the topological insulator Bi<sub>2</sub>Te<sub>3</sub>, *Physical Review B* **92**, 014301 (2015).
- [17] A. Levchuk, B. Wilk, G. Vaudel, F. Labbé, B. Arnaud, K. Balin, J. Szade, P. Ruello, and V. Juvé, Coherent acoustic phonons generated by ultrashort terahertz pulses in nanofilms of metals and topological insulators *Physical Review B* **101**, 180102(R) (2020).
- [18] See Supplemental Material at <http://link.aps.org/supplemental/>
- [19] P. B. Allen, Theory of thermal relaxation of electrons in metals, *Physical Review Letters* **59**, 1460 (1987).
- [20] B. Arnaud and Y. Giret, Electron Cooling and Debye-Waller Effect in Photoexcited Bismuth, *Physical Review Letters* **110**, 016405 (2013).
- [21] W. Richter, H. Köhler and C.R. Becker, A Raman and Far-Infrared Investigation of Phonons in the Rhombohedral V<sub>2</sub>VI<sub>3</sub> Compounds, *phys. stat. sol. (b)* **84**, 619 (1977).
- [22] C. Wang, X. Zhu, L. Nilsson, J. Wen, G. Wang, X. Shan, Q. Zhang, S. Zhang, J. Jia, and Q. Xue, In situ Raman spectroscopy of topological insulator Bi<sub>2</sub>Te<sub>3</sub> films with varying thickness, *Nano Research* **6**, 688-692 (2013).
- [23] A. A. Melnikov, K. N. Boldyrev, Y. G. Selivanov, V. P. Martovitskii, S. V. Chekalin, and E. A. Ryabov, Coherent phonons in a Bi<sub>2</sub>Se<sub>3</sub> film generated by an intense single-cycle THz pulse, *Physical Review B* **97**, 214304 (2018).
- [24] Y. Giret, A. Gellé and B. Arnaud, Entropy driven atomic motion in laser-excited bismuth, *Physical Review Letters* **106**, 155503 (2011).
- [25] S. M. O'Mahony, F. Murphy-Armando, E. D. Murray, J. D. Querales-Flores, I. Savić, and S. Fahy, Ultrafast Relaxation of Symmetry-Breaking Photo-Induced Atomic Forces, *Physical Review Letters* **123**, 087401 (2019).
- [26] D. Sangalli and A. Marini, Ultra-fast carriers relaxation in bulk silicon following photo-excitation with a short and polarized laser pulse, *Europhy. Lett.* **110**, 47004 (2015).
- [27] J. Sjakste, K. Tanimura, G. Barbarino, L. Perfetti and N. Vast, Hot electron relaxation dynamics in semiconductors: assessing the strength of the electron-phonon coupling from the theoretical and experimental viewpoints, *J. Phys. Condens. Matter* **30**, 353001 (2018).
- [28] X. Tong and M. Bernardi, Toward precise simulations of the coupled ultrafast dynamics of electrons and atomic vibrations in materials, *Phys. Rev. Research* **3**, 023072 (2021).
- [29] M. Kozina, M. Fechner, P. Marsik, T. van Driel, J. M. Glowina, C. Bernhard, M. Radovic, D. Zhu, S. Bonetti, U. Staub and M. C. Hoffmann, Terahertz-driven phonon upconversion in SrTiO<sub>3</sub>, *Nature Physics* **15**, 387-392 (2019).
- [30] M. H. Francombe, Structure cell data and expansion coefficients of bismuth tellurium, *J. Appl. Phys.* **9**, 415 (1958).
- [31] J. O. Jenkins, J.A. Rayne and R. W. Ure, Elastic Moduli and Phonon Properties of Bi<sub>2</sub>Te<sub>3</sub>, *Physical Review B* **5**, 3171 (1972).
- [32] R. Busselez, A. Levchuk, P. Ruello, V. Juvé and B. Arnaud, Anisotropy in the dielectric function of Bi<sub>2</sub>Te<sub>3</sub> from first principles: From the UV-visible to the infrared range, *Physical Review B* **107**, 174305 (2023).
- [33] C. Hartwigsen, S. Goedecker, and J. Hutter, Relativistic separable dual-space Gaussian pseudopotentials from H to Rn, *Physical Review B* **58**, 3641 (1998).
- [34] X. Gonze, B. Amadon, P.-M. Anglade, J.-M. Beuken, F. Bottin, P. Boulanger, F. Bruneval, D. Caliste, R. Caracas, M. Côté *et al*, ABINIT: First-principles approach to material and nanosystem properties, *Comput. Phys. Commun.* **180**, 2582 (2009).
- [35] X. Gonze, F. Jollet, F. Abreu Araujo, D. Adams, B. Amadon, T. Applencourt, C. Audouze, J.-M. Beuken, J. Bieder, A. Bokhanchuk *et al*, Recent developments in the ABINIT software package, *Comput. Phys. Commun.* **205**, 106 (2016).
- [36] X. Gonze, First-principles responses of solids to atomic displacements and homogeneous electric fields: Implementation of a conjugate-gradient algorithm, *Physical Review B* **55**, 10337 (1997).

- [37] W. Richter, H. Köhler and C.R. Becker, A Raman and Far-Infrared investigation of phonons in the rhombohedral  $V_2VI_3$  compounds *phys. stat. sol. (b)* **84**, 619 (1977).
- [38] I. Souza, J. Iñiguez and D. Vanderbilt, First-principles Approach to Insulators in Finite Electric Fields, *Physical Review Letters* **89**, 117602 (2002).
- [39] Kwan-Woo Lee and W. E. Pickett, Born effective charges and infrared response of LiBC, *Physical Review B* **68**, 085308 (2003).
- [40] M. Born and K. Huang, *Dynamical Theory of crystal lattices*, Oxford Classic Texts in the Physical Sciences (Clarendon Press, 1988).
- [41] P. G. Radaelli, Breaking symmetry with light: Ultrafast ferroelectricity and magnetism from three-phonon coupling, *Physical Review B* **97**, 085145 (2018).
- [42] S. Maehrlein, A. Paarmann, M. Wolf, and T. Kampfrath, Terahertz Sum-Frequency Excitation of a Raman-Active Phonon, *Physical Review Letters* **119**, 127402 (2017).
- [43] D. M. Juraschek and S. F. Maehrlein, Sum-frequency ionic Raman scattering, *Physical Review B* **97**, 174302 (2018).
- [44] Courtney L. Johnson, Brittany E. Knighton, and Jeremy A. Johnson, Distinguishing Nonlinear Terahertz Excitation Pathways with Two-Dimensional Spectroscopy, *Physical Review Letters* **122**, 073901 (2019).
- [45] M. Janek, I. Bugár, D. Lorenc, V. Szöcs, D. Velič, and D. Chorvát, Terahertz time-domain spectroscopy of selected layered silicates, *Clays Clay Miner.* **57**, 416-424 (2009).
- [46] R. Vilaplana, O. Gomis, F. J. Manjón, A. Segura, E. Pérez-González, P. Rodríguez-Hernández, A. Muñoz, J. González, V. Marín-Borrás, V. Muñoz-Sanjosé, C. Drasar, and V. Kucek, High-pressure vibrational and optical study of  $Bi_2Te_3$ , *Physical Review B* **84**, 104112 (2011).
- [47] A. Marini, C. Hogan, M. Grüning, D. Varsano, Yambo: an ab initio tool for excited state calculations, *Comput. Phys. Commun.* **180**, 1392 (2009).
- [48] D. Sangalli, A. Ferretti, H. Miranda, C. Attaccalite, I. Marri, E. Cannuccia, P. Melo, M. Marsili, F. Paleari, A. Marrazzo, G. Prandini, P. Bonfà, M. O Atambo, F. Affinito, M. Palumbo, A. Molina-Sánchez, C. Hogan, M. Grüning, D. Varsano and A. Marini, Many-body perturbation theory calculations using the yambo code, *Journal of Physics: Condensed Matter* **31**, 325902 (2019).
- [49] B. Arnaud and M. Alouani, Local-field and excitonic effects in the calculated optical properties of semiconductors from first-principles, *Physical Review B* **63**, 085208 (2001).
- [50] H. Bando, K. Koizumi, Y. Oikawa, K. Daikohara, V. A. Kulbachinskii and H. Ozaki, The time-dependent process of oxidation of the surface of  $Bi_2Te_3$  studied by x-ray photoelectron spectroscopy, *J. Phys.: Condens. Matter* **12**, 5607 (2000).
- [51] C. C. Katsidis and D. I. Siapkas, General transfer-matrix method for optical multilayer systems with coherent, partially coherent, and incoherent interference, *Applied Optics* **41**, 3978 (2002).
- [52] V. Dolocan and F. Iova, Optical properties of  $Bi_2O_3$  thin films, *Phys. Stat. Sol. (a)* **64**, 755 (1981)
- [53] N. Uchida, Optical Properties of Single-Crystal Paratellurite ( $TeO_2$ ), *Physical Review B* **4**, 3736 (1971).
- [54] R. Nitsche and T. Fritz, Precise determination of the complex optical constant of mica, *Applied Optics*, Vol. **43**, No. 16, p. 3263-3270 (2004).